Shake table tests on 1:2 reduced scale masonry house with the application of horizontal seismic bands

Santosh Yadav, Yannick Sieffert, Florent Vieux-Champagne, Yann Malecot, Majid Hajmirbaba, Luis Arléo, Eugénie Crété, Philippe Garnier

Shake table tests on 1:2 reduced scale masonry house with the application of horizontal seismic bands

Santosh Yadav[1]*, Yannick Sieffert[1], Florent Vieux-Champagne[1], Yann Malecot[1], Majid Hajmirbaba[2], Luis Arléo[2], Eugénie Crété[2], and Philippe Garnier[2]

[1]*Univ. Grenoble Alpes, Grenoble INP, CNRS, 3SR,38000 Grenoble, France*

[2] *Laboratoire CRAterre, Unité de recherche AE&CC, École Nationale Supérieure d'Architecture de Grenoble, Grenoble, France*

*Email: yadv.santos@gmail.com ; http://orcid.org/0000-0002-4239-8518

Shake table tests on 1:2 reduced scale masonry house with the application of horizontal seismic bands

Abstract

The safety of people's lives is crucial in structures that provide shelter. Earthquakes are a major natural disaster that have claimed thousands of lives over the years, but other factors can also cause damage to these structures. Building collapses are often due to their inability to endure the seismic loading, not the earthquake itself. Most residential buildings are masonry structures. There are many strategies for enhancing structural behavior, but very little research has been done on masonry structures, which house about 1/3rd of the world's population. This study focuses on characterization of seismic response using shake table tests to assess the dynamic behavior of masonry structures when horizontal seismic bands are applied. Horizontal seismic band is one of the traditional techniques used in masonry structure. Three reduced scale models were constructed with one using a reinforced concrete band, one with a timber band, and one without a band. All models were constructed using extruded earth block and mud mortar, common building materials in developing nations. The models were tested on a shake table using the same loading signal to compare their response behavior. A high-speed camera was also used to capture images; accelerometers and displacement sensors were installed to record the response. Digital Image Correlation (DIC), which provides non-contact optical measurement, has been essential in obtaining full-field measurement. The results showed significant improvement in the seismic response of structures with horizontal seismic bands. The behaviors are compared in terms of natural frequency, damping, energy dissipation, and crack propagation patterns using two types of materials as seismic bands.

Keywords: Earth masonry; reinforcement; traditional construction; dynamic test;

a reduced scale model; Digital Image Correlation; shake table

1. Introduction

A house is a basic need for a human, providing shelter and protection during natural disasters such as earthquakes. Earthquakes often come without warning and cannot be prevented, leading to loss of life each year. The phrase "earthquakes don't kill people, buildings do", which was observed in areas with seismically vulnerable structures such as during an earthquake in Bam (Nadim et al., 2004), in Lesvos (Vlachakis & Kleanthi, 2020), in Nepal (Gautam, Rodrigues, Bhetwal, Neupane, & Sanada, 2016). Many houses in developing nations are constructed from bio- and geo- based local materials (Bhanulatha, 2018; Gülkan & Langenbach, 2004; Shrestha, Pradhan, & Guragain, 2012). Masonry structures are most widely used as residential building, which accounts to provide shelter to more than 1/3rd of the world population (Barbacci, 2020).
The primary concern for any building is to prevent collapse during disasters and save lives. There are many examples where traditional constructions have outperformed during earthquake events (Langenbach, 2002; Liang, Stanislawski, & Hota, 2011). But, the lack of transfer of the traditional construction practice and haphazard modification of the old structures increased the structural vulnerability (Khadka & Shakya, 2021). Learning from the past traditional practice and understanding the science behind them can help us to address challenges faced in the field. Many seismic strengthening techniques are available to enhance the performance of masonry structures, such as the use of polypropylene band mesh (Banerjee, Nayak, & Das, 2021; Sathiparan, Mayorca, & Meguro, 2012), nylon straps (Blondet, Tarque, & Vargas, 2018), TRM (Textile Reinforced Mortars) or FRP (Fiberglass Reinforced Polymer) (Dalalbashi, Ghiassi, & Oliveira, 2021; Papanicolaou, Triantafillou, Karlos, & Papathanasiou, 2007), the horizontal seismic band (Ortega, Vasconcelos, & Correia, 2015), and many others. All these techniques have been proven to improve the strength, global stiffness and damage tolerance of masonry buildings. Glass based TRM or FRP materials have considerable impact on the in-plane wall but their effect are less pronounced in out-of-plane wall due to the tension compression stresses introduced in the system (Dalalbashi et al., 2021). The application of any of these techniques must be practical and sustainable for the given location. For this study, the application of horizontal seismic band in masonry is considered, which is recommended by the building code of Nepal (DUDBC, 2015; NBC203, 2015) and also used in several countries in Asia, and South America.

2. Rationale of the study

Seismic bands are a traditional constructive technique specific to masonry structures in a seismic zone (the first traces go back to the Minoan period 3500 BC (Ortega et al., 2015)) and are still used in several parts of the world (Hofmann, 2015). Historically, seismic bands were made of timber or long pieces of stone. However, in recent construction, timber, reinforced concrete (RC), and bamboo are used as seismic band materials. The recommendation for the location and placement of such bands varies depending upon the guidelines. The placement of bands is recommended at lintel, roof, and gable levels as per (Arya et al., 2004; IS13828, 1993). Whereas (UN-Habitat, L'urgence and NSET-Nepal, 2006; DUDBC, 2015; NBC203, 2015) recommend placing such bands at the sill, plinth, and intermediate levels between sill and lintel level along with lintel, roof, and gable band.
The use of seismic bands improves the resilience of masonry structures. Quasi-static tests performed on masonry walls with timber seismic band highlighted its advantages in controlling crack propagation and increasing the peak shear resistance (Aranguren, Vieux-champagne, Duriez, & Aubert, 2020; Wang et al., 2017). The crack opening rate also varies with the application of a seismic band as compared to one without a band (Yadav et al., 2021). Numerical model study carried out on masonry structure with the application of seismic bands demonstrated a gradual enhancement in their global box like behavior (Adhikari, Vatteri, & D'Ayala, 2023). Dynamic tests performed on a shake table with stone masonry using an RC band and timber band with containment mesh helped enhance the structure's performance, where both structures survived a Peak Ground Acceleration (PGA) of 1g (Bothara, Ahmad, Ingham, & Dizhur, 2019). The energy dissipation at the interface between the mortar joint and the seismic band material was

studied using the quasi-static cyclic test, where the energy dissipated by the RC band was observed to be the highest (Yadav, Sieffert, Crété, Vieux-Champagne, & Garnier, 2018). These results indicate benefits of using seismic bands, but selecting a material remains a challenge as cost and availability vary. The performances of different materials were studied with the help of quasi-static tests by various researchers, however their impact in the dynamic loading is limited and remains unexplored. Therefore, in this study, the timber and reinforced concrete (RC) band were used to make a comparative study at a house scale to understand the overall structural behavior using actual seismic loading. The details of the experimental setup, specimen preparation, testing protocols, methodology, and results are presented in the paper.

3. Experimental setup

3.1. Dynamic similitude

During shake table tests, where prototype response is non-linear, scaled stresses in models may overestimate prototype resistance. To ensure reliable results, dynamic similarity must be maintained. However, full-scale models are often infeasible due to shake table limitations and cost, so reduced-scale models are commonly used. A complete similarity in geometry, materials properties, and loading must be made to avoid the size effect (Harris & Sabnis, 1999). Several dynamic similitude laws are available and used for the dynamic test on masonry structures. Petry & Beyer (2014) used the Artificial Mass Simulation Scaling law, (Rafi, Lodi, Qazi, Kumar, & Verjee, 2018) used Buckingham's Pi theorem, and (Wang, Liu, Guragain, Shrestha, & Ma, 2018) used Cauchy & Froude law.

The stress scaling ratio between the reduced-scale model and the prototype must be unity to maintain dynamic similitude. In practice, the same materials are used for both the model and the prototype. To achieve the same stress level, the density of the materials in the reduced-scale model must be increased. However, this is not always possible. In such cases, additional mass can be added to the model to modify its mass without affecting its dimensions or stiffness. (Petry & Beyer, 2014) and (Wang et al., 2018) used an additional dead load to equalize the stress scaling ratio. But, in case the application of the additional mass is not possible, then the Cauchy similitude law can be used (Banerjee et al., 2021; Ghezelbash, Beyer, Dolatshahi, & Yekrangnia, 2020; Mendes, Lourenço, & Campos-Costa, 2013).

In general, the model's material is the same as that of the prototype, so the Cauchy law can be used to make sure the accelerations in the model are equal to the scale factor times the accelerations in the prototype. The accelerations applied to the shake table can be adapted depending on the scaling factor, but it is impossible to scale the acceleration due to gravity. For the shake table test, a 1:2 reduced scale model was selected, and the Cauchy law was applied to maintain dynamic similarity, as adding an additional mass of 4 tons was not feasible. Additionally, the material used in building the model was geometrically scaled, but no adjustments were made to the mechanical properties. This was due to the primary goal of the study being to compare the structural response under seismic band applications and if the same material was utilized in all three models, the results could be compared. Table 1 summarizes the similarity scale factors for various parameters for the 1:2 reduced scale model.

Table 1 Dynamic similitude scaling factor for 1:2 reduced scale model

Parameter	Scaling notation	Equation	Scale Factor	Scaling factor
Length (L)	λ_L	$\lambda_L = L_p/L_m = \lambda$	λ	2.0
Density (ρ)	λ_ρ	$\lambda_\rho = \rho_p/\rho_m$	1	1.0
Mass (m)	λ_m	$\lambda_m = \lambda_V \times \lambda_\rho$	λ^3	8.0
Linear displacement (d)	λ_d	$\lambda_d = \lambda_L$	λ	2.0

Velocity (v)	λ_v	$\lambda_v = v_p/v_m$	1	1.0
Acceleration (a)	λ_a	$\lambda_a = a_p/a_m = t_m/t_p$	λ^{-1}	0.5
Weight (W)	λ_W	$\lambda_W = \lambda_L^3 \times \lambda_\rho$	λ^3	8.0
Shear Force (F)	λ_F	$\lambda_F = \lambda_L^3 \times \lambda_\rho \times \lambda_a$	λ^2	4.0
Time (t)	λ_t	$\lambda_t = L_p/L_m \times \lambda_v$	λ	2.0

* p = prototype; m = model; λ_V = Volume

3.2. Shake table

The uniaxial shake table facility available at FCBA, Bordeaux, was used for conducting the dynamic tests. A 250 kN servo-hydraulic actuator operates the 6 × 6 m^2 surface area aluminum platform. The shake table's maximum acceleration, velocity, and displacement capacity are 4g, 0.75 m/s, and ± 0.125 m, respectively.

The advantage of the shake table dynamic test is that it allows researchers to study the effects of earthquakes on structures by simulating actual earthquake signals. The Guadeloupe ground motion, a modified natural accelerogram adapted from the Miyagi earthquake (Japan 2003), measured at the K-Net station and calibrated to have improved spectrum representativeness (Florent Vieux-Champagne, 2013) was used as an input earthquake signal.

The Guadeloupe earthquake signal was taken from (Boudaud, Baroth, & Daudeville, 2016; F. Vieux-Champagne et al., 2017) and applied the Cauchy similitude law. Five loadings at 112%, 194%, 240%, 273%, and 386% of Guadeloupe (GUA) signal were used for the test. These signal levels are not round numbers due to the feedback mechanism from the hydraulic loading actuator. The maximum Peak Ground Acceleration (PGA) applied during the test corresponds to 1.275g and earthquake magnitude of 7.8 at the prototype scale (real scale house). The displacement-time series signal at 194% of Guadeloupe is shown in Fig. 1 and the applied Guadeloupe signal and actual PGA values are summarized in Table 2.

Table 2 Summary of applied Guadeloupe signal and the corresponding PGA values

Loading sequence	Measured PGA, g	% GUA
1	0.74	112%
2	1.28	194%
3	1.58	240%
4	1.80	273%
5	2.55	386%

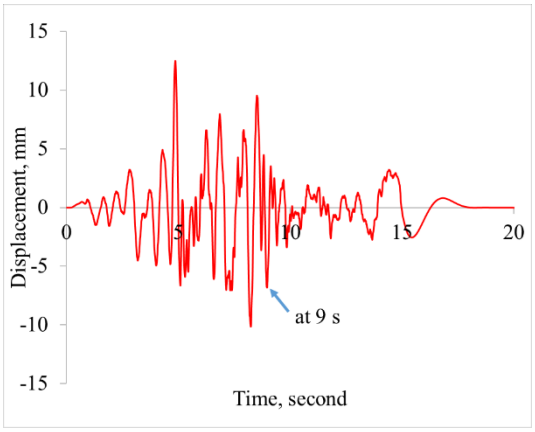

Fig. 1. Shake table time-displacement series at 194 GUA

3.3. Specimen preparation

The extruded earth block of dimensions 175 mm × 125 mm × 50 mm was custom ordered from La Brique de Nagen for the building 1:2 reduced scale models of a two-room earth masonry house. The dimensions of the actual scale house were taken from Based on Nepal's DUDBC reconstruction guidelines (DUDBC, 2015), the reduced scale model was constructed using the dynamic similitude law. The dimensions of openings and seismic bands were also taken from the same guidelines, and the overall dimensions were adjusted to fit the shake table platform.

The external dimension of the reduced scale house was 3230 mm × 1575 mm (see Fig. 2). The house was made symmetric along the loading direction with two windows and three-door

openings to minimize the torsional effect on the structure. The dimension of the mortar joint was 10 mm, assuming the mortar thickness in the prototype to be 20 mm, the maximum thickness recommended (NBC203, 2015). Three reduced scale models were built simultaneously: model 1 without a band, model 2 with a timber seismic band, and model 3 with an RC seismic band. The seismic band dimensions followed the similitude law, except for the RC band's rebar size, which was set at the minimum dimension available in France (8 mm main rebar and 6 mm tie rebar).

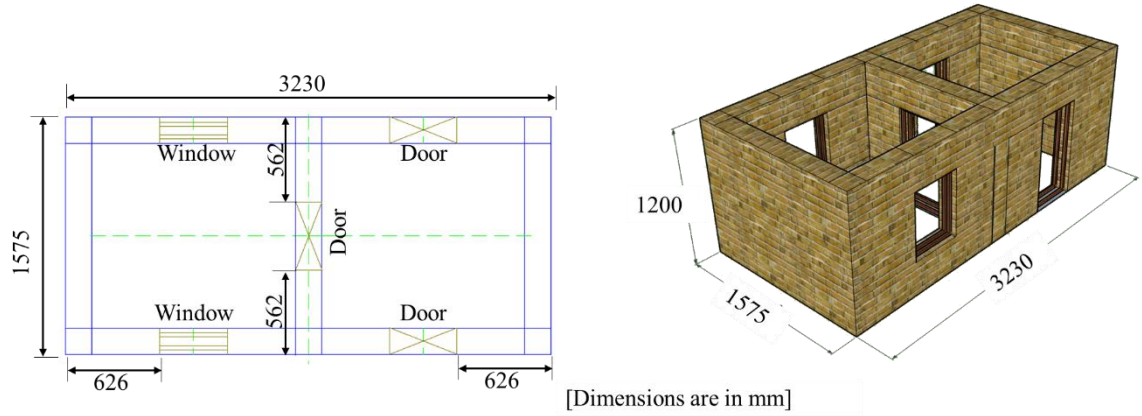

Fig. 2. Model building layout plan details (left) and an isometric representation (right)

Fig. 3 illustrates the common construction stages for all three models. In the beginning, approximately 30 mm-thick plain concrete was cast on the metallic part, leaving the top 20 mm for the first layer of extruded earth block to prevent sliding at the interface between concrete and mortar. The three-door frames were installed before laying the first layer, as shown in Fig. 3 (center). To avoid settling due to self-load, the number of layers built per day was limited to 3-4 courses. The dimensions of the door and the window are 0.45 m × 0.90 m and 0.45 m × 0.60 m, respectively.

Fig. 3. Construction stages for the model house

A total of four seismic bands were used for the model with a seismic band, located at the sill, intermediate, lintel, and roof level (see Fig. 3 house with timber band). The placement of the timber seismic band at sill level is shown in Fig. 4a, and Fig. 4b depicts the formwork for the casting the RC band. The three reduced-scale buildings were left to dry at a room temperature of 23 ± 2 °C and relative humidity of 50 ± 5%. The detail of the metal base frame and steps to displace the model house from the floor level to the shake table surface can be found in Yadav et al. (2022).

The roof truss was made with timber and covered with galvanized iron (GI) sheet, as seen in Fig. 5. The roof was secured in place with 11 metal cables- 8 along the in-plane wall and 3 on the out-of-plane wall, passed through the lintel level and pre-stressed. The location of the metal cable and the connection detail are shown in Fig. 5. The GI sheet on the front part was made shorter to avoid shadow formation during the Digital Image Correlation (DIC) imaging. The same roof truss was used for all houses as it was not damaged during the loading. The total mass of the roof was approximately 130 kg.

Fig. 4. Placement of timber band (a) and RC band (b)

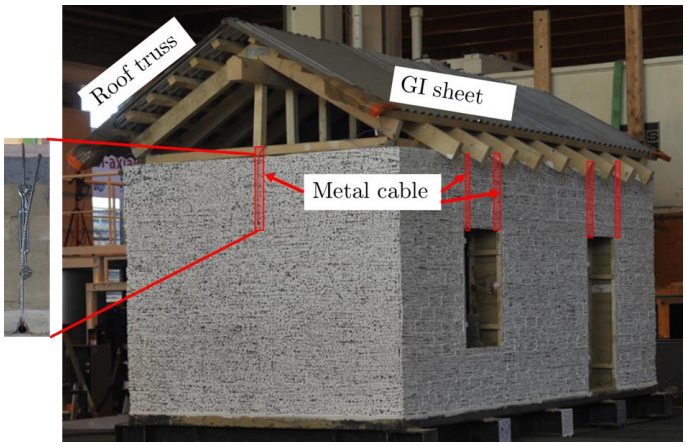

Fig. 5. Roof truss and connection with house model

3.4. Material characterization

The compression test was conducted on 7 extruded earth block units (175 mm x 125 mm x 50 mm), in the vertical orientation. The mud mortar was made with 2:1 (soil: sand) mixture and three cylindrical samples (diameter = 66 ± 1 mm, height = 126 ± 2 mm) were tested under compression loading.
The flexural test was carried out on 6 extruded earth block units using a three-point bending method. The material properties of the earth block unit and mud mortar are summarized in Table 3.

Table 3 Summary of material properties

	Extruded earth block			Mud mortar		
	Average	SD	CoV	Average	SD	CoV
Compressive strength, MPa	3.18	0.86	26.9%	2.10	0.22	11.0%
Secant Modulus, E_{peak}, MPa	433.10	163.80	37.8%	427.00	127.00	30.0%
Flexural strength, MPa	2.55	0.36	14.0%			

NOTE: SD = Standard Deviation; CoV = Covariance

A sandwich shear test was carried out to assess the quality of the mortar joint at the interface (Bothara & Brzev, 2011). To determine the shear resistance of the interface, three sandwich specimens were prepared using extruded earth block and mortar, and three samples were prepared using extruded earth block-concrete brick sandwiched with mortar. Due to the weak interface between the earth block and mortar, a simplified testing technique involving bucket loading tests (Duriez, Vieux-Champagne, Trad, Maillard, & Aubert, 2020) was utilized.
The maximum force at the failure of the interface was recorded for each test. The shear resistance was calculated by dividing the maximum force by the contact area. This resistance is solely attributed to the cohesive bond as no pre-compression loading was applied during the test. Table

4 summarizes the shear resistance values for different interfaces. For the extruded earth block samples, the shear resistance was found to be 6.02 MPa, which is close to the cohesion value, c = 14 - 15 kPa obtained for similar extruded earth blocks (Duriez et al., 2020; Reyes et al., 2019).

Table 4 Summary of shear resistance at the interface

Sample description	Average shear resistance, kPa	SD	CoV
Extruded-mortar-Extruded	6.02	2.80	46.5%
Extruded-mortar-concrete	8.43	2.05	24.3%

The failure occurred at the interface between the mortar joint and block unit, but never within the mortar joints. A similar pattern of failure was observed in the extruded earth block specimens tested under shear loading (Lan, Wang, Xin, & Liu, 2020).

The characteristic shear strength of masonry for solid clay brick and general-purpose mortar can be estimated using Equation 1 (Eurocode-6, 2005), which is based on the Mohr-Coulomb law of friction. This equation provides an approximation of the characteristic shear strength of masonry at various design compressive stress values. The coefficient value of 0.4, which represents the contribution of the shear strength due to compressive stress in the wall, is used as a constant for all types of masonry (Tomaževič, 2009) in cases where the frictional coefficient is unknown. However, the friction angle obtained from the shear test experiment at various normal stress using extruded earth block from same manufacturer and mud mortar was found to be 42° (Duriez et al., 2020). Given this friction angle, the coefficient value for frictional contribution to the shear strength would be 0.9 instead of 0.4 in Equation 1, which is close to the average coefficient of friction between brick and masonry used in the numerical model by (Gaetano et al., 2022).

$$f_{vk} = f_{vk0} + 0.4\sigma_d \tag{1}$$

Where f_{vk}= characteristic shear strength of masonry

f_{vk0} = initial shear strength, under zero compressive stress

σ_d = design compressive stress perpendicular to the shear in the member at the level under consideration

The mechanical properties of materials are crucial in verifying numerical models and conducting extensive parametric analyses. However, as highlighted by Castellano et al.(2023), the results of sensitivity analyses indicate that only those parameters that determine the failure mode have a significant impact on the overall behavior of the model. The choice of parameters for a numerical model is dependent on the type of model, approach, and objectives of the study, and it may not always be feasible to determine all the mechanical properties, particularly in terms of strength, stiffness, and toughness under various loading conditions, such as compression, bending, and shear. To address the challenge of limited experimental data, Jafari, Rots, & Esposito (2022) present a correlation between various material properties using data from laboratory tests and specimens extracted from unreinforced masonry structures built between 1910 and 2010 in the Netherlands.

3.5. Instrumentation and measurement sensor

3.5.1. Accelerometer and displacement sensor

Accelerometer and Drawing Wire Displacement Sensor (DWDS) were utilized to measure the acceleration and displacement values on a house model at various locations. As shown in Fig. 6 (a), four bidirectional accelerometers were positioned at the corner (BA_{1-4}) and one monodirectional accelerometer (MA) on the ridge beam of the roof truss. Another accelerometer was placed at the mid-height of the wall. There was no significant acceleration along the orthogonal direction, so it was not used for analysis purposes. The acceleration readings obtained from the bidirectional accelerometers along the loading direction were analyzed.

Similarly, seven DWDS were positioned, as shown in Fig. 6 (a) with D_1 on the ridge beam, $D_{2\text{-}5}$ at the seismic band level on the out-of-plane (OOP) wall, and $D_{6\text{-}7}$ at the OOP wall corner at roof band level.

3.5.2. Imaging setup for DIC

Digital Image Correction (DIC) is a potent tool to assess the displacement field information without direct sensor placement on the specimen. The general schematic layout for the dynamic test setup is shown in Fig. 6 (b). The house model's longer wall was parallel to the shake table's loading direction. A high-speed camera was positioned to face the in-plane, with proper lighting provided by a luminous spotlight.

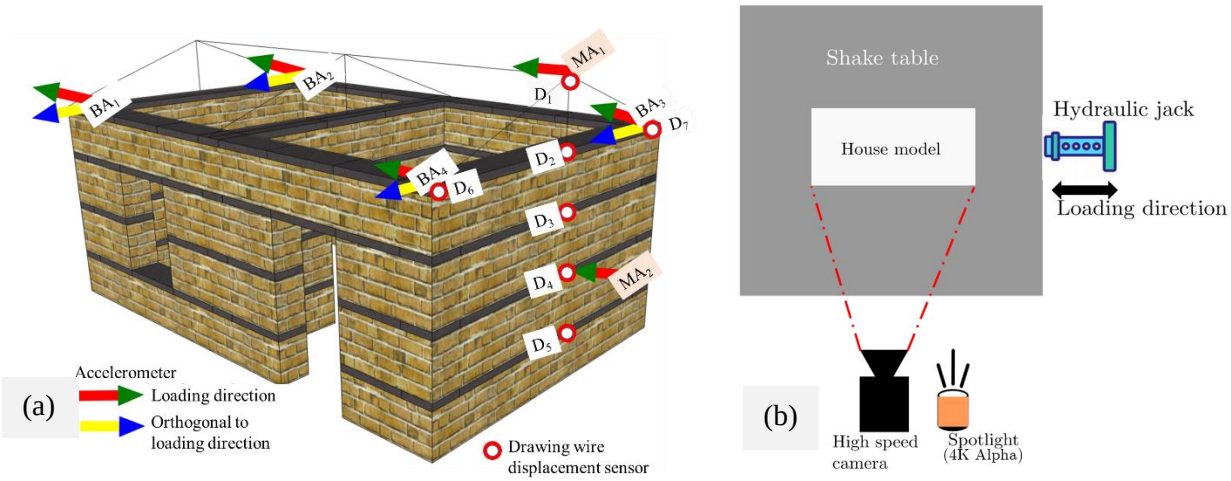

Fig. 6. Placement of measuring sensors on the model (a) and camera setup (b)

A single high-speed camera, Phantom V2640, was used to capture the image at 1000 fps. The technical specifications of high-speed are listed in Table 5.

Table 5 Technical specification of high-speed camera

High-speed camera	Characteristics
Brand/model	Phantom V2640
Resolution	2048 × 1944 px
Frequency	1000 fps
Time recorded	25 seconds for each signal
Lens	Nikkor Ai-S 28 mm f/2
Sensor size, mm	27.6 × 26.3
Distance from the wall	6.0 m
Resolution scale	Range between 1.86 and 1.88 mm/px

Proper lighting is crucial to ensure proper exposure on the specimen surface and to capture images with low ISO levels to minimize noise. A 4000W 4K alpha spotlight was positioned at 7 m from the in-plane wall surface for optimal lighting. The technical specifications for the 4K alpha spotlight are listed in Table 6.A high ballast frequency was utilized to eliminate flicker during image acquisition.

Table 6 Technical specification for 4K alpha spotlight

Lighting	Technical characteristics
Brand/model	4 K alpha version
Power	4000W
Frequency ballast	1000 Hz
Color temperature	5600K
Option	shallow alpha
lamp	Open-Eyes HMI, ceramic G38 socket

3.5.3. Validation of DIC

The main principle of the DIC technique is the tracking of the random pattern defined by a gray value by comparing one image to another. For optimal results, speckle patterns should be 3-8 pixels in size (Salmanpour & Mojsilović, 2013). On smaller surfaces with high-resolution cameras, speckle patterns can be created with an aerosol can paint (Castillo, Allen, Henry, Griffith, & Ingham, 2019; Stazi et al., 2020). However, for the large (3230 mm × 1200 mm) in-plane walls of the model house and the low camera resolution, an efficient approach was needed. The random patterns can also be created with acrylic paint by projecting it by the dynamic shocking movement of the wrist using a brush (Sieffert et al., 2016). However, this method was deemed too labor-intensive for the three model houses and therefore, an efficient approach was required and developed.

To prepare the wall surfaces, any loose particles were cleaned with a dry cloth, then two coats of white mat paint were applied to provide proper contrast. After drying for a couple of hours, an array of cotton buds was prepared, as shown in Fig. 7, and used to stamp black dots on the wall surface with mat black paint to avoid glossy reflections. This array expedited the process, and the black dots' density was later increased using single cotton buds. The grayscale image histogram for the speckle pattern surface had two peaks, as shown in Fig. 8, indicating even black and white distribution.

Fig. 7 Arrangement of cotton bud for application of black speckles pattern

Fig. 8 Grayscale image histogram for speckle pattern on the wall surface

Fig. 9 shows the grayscale image for a speckle pattern with 30 x 30 pixels at various zoom levels. The 30 x 30 pixels subset has high contrast for the random patterns and consists of several points. The speckle dimension ranges from 3 to 6 pixels in size (Fig. 9 (c)).

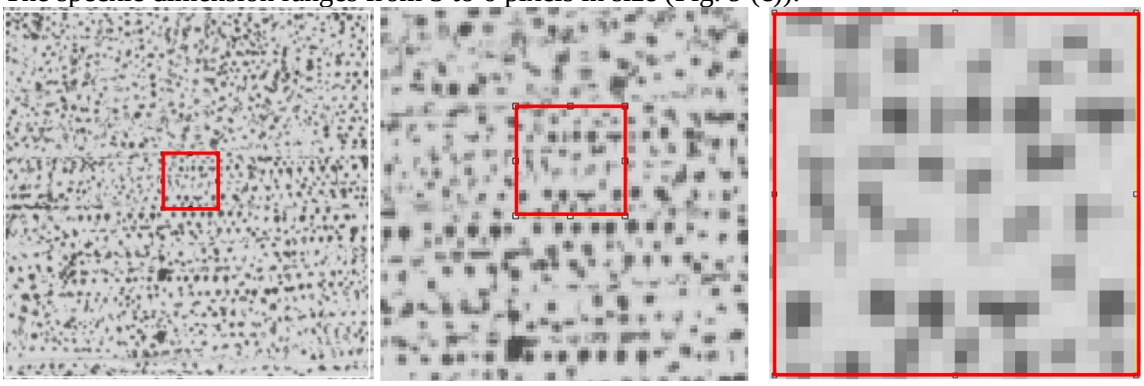

a)Image size: 200 x 200 pixels b)Image size: 100 x 100 pixels c)Image size: 30 x 30 pixels

Fig. 9. Grayscale of sample speckle pattern with a 30 × 30 subset at different zoom levels

The GOM correlates 2D software was utilized to analyze the high-speed camera images. The image captured from the camera was converted into a grayscale image, then imported into the software for calculation. The 30 x 30-pixel subset/facet and a point distance of 15 pixels were

applied to all the models. The resolution scale ranged between 1.86 to 1.88 mm/px. The accuracy of GOM correlate measurement was confirmed by analyzing the images taken before testing, which had a mean noise level of 0.012 mm and was within the acceptable deviation of the 0.01 pixels using bicubic subpixel interpolation.

The DIC output for field displacement was validated against the LVDT results for table displacement. A point on the metal frame (as indicated in Fig. 10) was selected, and the absolute displacement was extracted. The comparison of the table displacement from LVDT and DIC was made in the time-series domain (Fig. 10) and in the frequency domain using Fast Fourier Transfer (Fig. 12 (a)) at 194 GUA. The results from DIC were found to be in good agreement with the LVDT results.

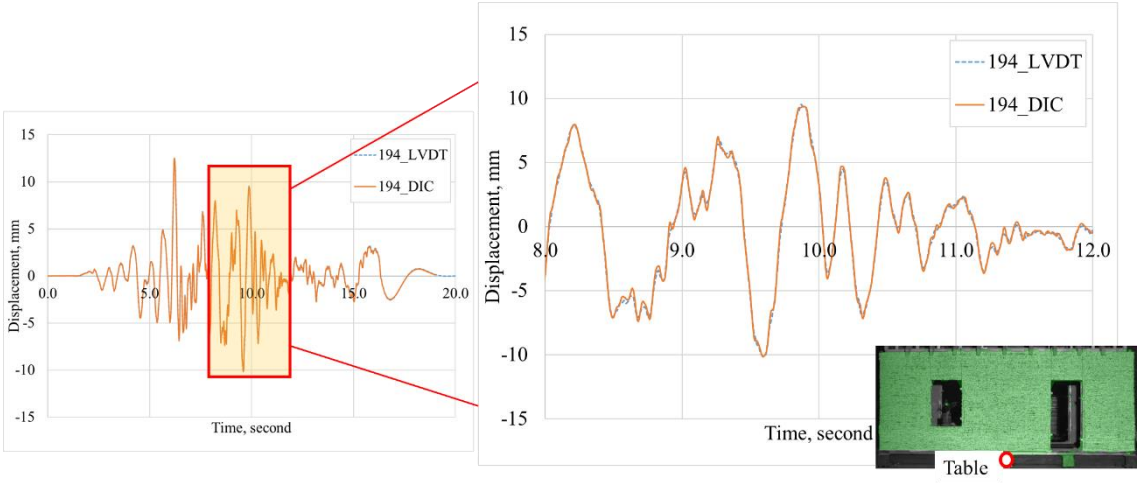

Fig. 10. Comparison of table displacement measured from LVDT and DIC in the time domain at 194 GUA

Similarly, the comparison for the relative displacement was also made. A point on the top right of the in-plane wall (see Fig. 11) corresponding to the location of DWDS6 is selected from the DIC output, and the relative displacement was calculated by subtracting the table displacement. Fig. 11 compares relative displacement at DWDS6 for the model with RC band at 194GUA signal in the time domain. Rel_DWDS6 indicates the relative displacement value obtained from the DWDS6 and shake table LVDT displacement. Rel_DWDS6_DIC indicates the relative displacement obtained from the DIC results. There is a slight difference in peak values due to different recording frequency of the data by DWDS (1024Hz) and DIC image (1000Hz).

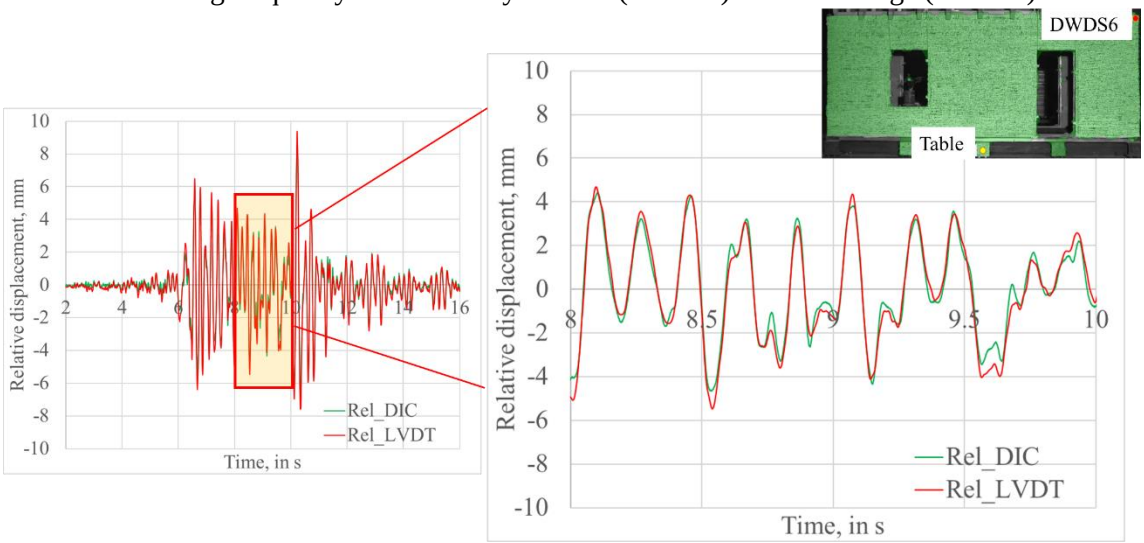

Fig. 11. Validation of DIC relative displacement for RC194 in the time domain

The comparison of relative displacement in the frequency domain (Fig. 12 (b)) shows good agreement between the results from DIC and DWDS6. This suggests that the subset size chosen

for DIC is appropriate for in-plane walls. Therefore, the DIC results for the displacement field are used for further analysis. The same validation process is applied to all other tests with varying signal magnitudes and house model.

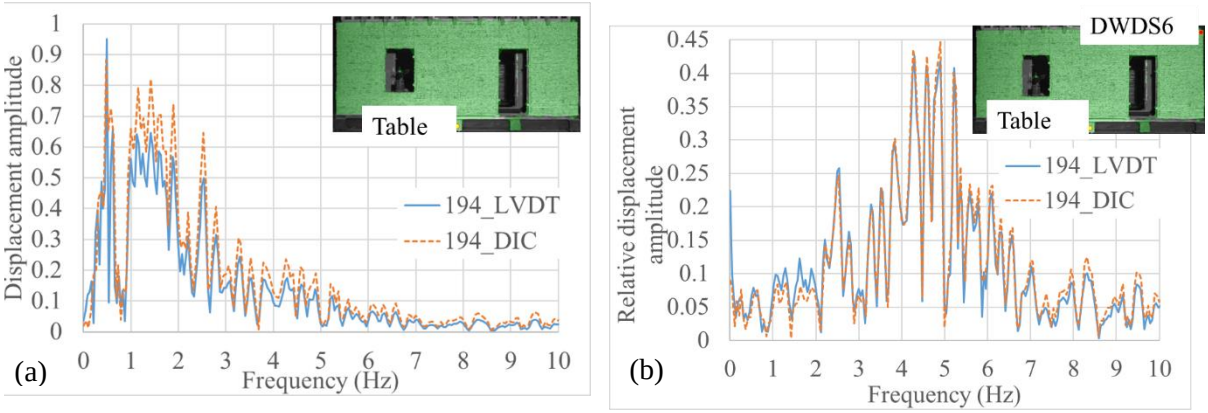

Fig. 12. Validation of (a) absolute and (b) relative displacement of shake table and RC model at GUA 194 in the frequency domain

4. Results and discussion

4.1. Global Structural behavior

4.1.1. Modal analysis

The equivalent SDOF system is defined by the equivalent stiffness, mass, height, and the modal participation factor during modal analysis. The frequency of the SDOF system represents the building's fundamental frequency. A random white noise signal was applied for modal analysis with root mean square amplitude of 0.3 mm and frequency range of 0.5 to 50 Hz. This type of noise has equal intensity at different frequencies, resulting in a constant power spectral density.
The white noise loading is used to perform the modal analysis and determine the structure's fundamental frequency before the test and the frequency drop in the structure after executing each seismic loading signal. Modal analysis was performed using Fourier analysis of input and output signals recorded using an accelerometer and force sensor, with the help of modal analysis instrumentation and software from Brüel & Kjær (BK). BK Connect Modal Analysis tool performs modal analysis from Frequency Response Function (FRF) acquired using the white noise excitation of the structure and provide corresponding fundamental frequency and equivalent viscous damping. FRF represents the ratio between output and input acceleration signals in the frequency domain.
The equivalent viscous damping ratio (EVDR) was determined using the half-power bandwidth method applied to the FRF peaks (Clough & Penzien, 2003; Papagiannopoulos & Hatzigeorgiou, 2011). The results of the model analysis for all three houses are summarized in Table 7. Mode 1 and 2 represents the flexural mode shape in in-plane and out-of-plane direction, with Mode 1 being the dominant mode for the seismic loading direction and used for result exploration in sections 4.1.2 and 4.2.1. Mode 3 represents the torsional mode shape at roof level. The fundamental frequency for the house with RC band, timber band, and without a band are 9.5, 11.6, and 18.4 Hz, respectively. The fundamental frequency is a function of mass and stiffness, and the mass of the three houses are approximately 4.3, 3.8, and 3.9 tons respectively for RC, timber, and without band house models. Although the difference in mass is not significant, the variation in the structure's stiffness caused by the application of seismic bands resulted in the change to the natural frequency of the structures.

Table 7 Summary of modal analysis results for the three model houses

Model	Mode	Frequency, Hz	Damping (%)	Mode shape
RC	1	9.5	18.2	In-plane flexural
RC	2	12.9	5.1	Out-of-plane flexural
RC	3	19.7	7.1	Roof torsion
Timber	1	11.6	21.1	In-plane flexural
Timber	2	13.5	4.9	Out-of-plane flexural
Timber	3	17.1	5.4	Roof torsion
Without	1	18.4	5.2	In-plane flexural
Without	2	26.3	4.3	Out-of-plane flexural
Without	3	29.8	3.1	Roof torsion

4.1.2. Fundamental frequency

The fundamental frequency of structures is determined by analyzing the peaks in Frequency Response Function (FRF) obtained from the accelerometer data recorded during the application of a random white noise signal after each loading signal. The FRF results from the test exhibit a wavy pattern as white noise signal contain frequency ranging from 0.5 to 50 Hz. This makes it difficult to accurately identify the peak at resonating frequency. To overcome this challenge, standardization was necessary. The Gaussian curve fitting approach was used to standardize the FRF results. With the help of Gaussian curve fitting (MATLAB tool), a smooth curve was obtained from discrete FRF point results, which was finally used to identify the fundamental frequencies. The frequency corresponding to the peak response gives the fundamental frequency of the structures. The average results from the four $BA_{1\text{-}4}$ measuring along the loading direction are used to obtain the house model's fundamental frequency after each loading signal. The variation in the fundamental frequency for each of the three house model is shown in Fig. 13, along the error bars are indicating the standard deviation (SD). The high SD for the house without a band at 273GUA is due to the wide crack in the walls, resulting in differences in displacement and frequency. The fundamental frequency of structure varies with the application of a seismic band. The natural frequency for the house without a band is declining at a faster rate, whereas for the houses with a seismic band, the change is gradual, and the rate of degradation is comparable. For 386GUA loading (house without a band), all the measurement sensors were removed because of the risk of collapse and sensor damage.

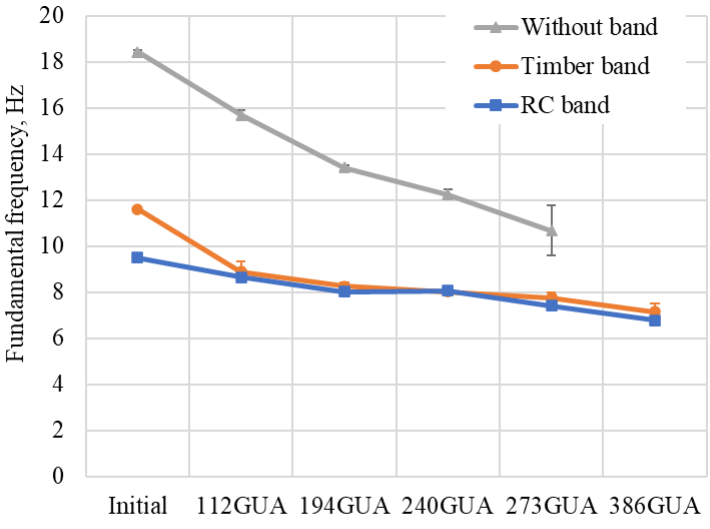

Standard deviation					
Without band	0.2	0.1	0.2	1.1	
Timber band	0.5	0.2	0.1	0.2	0.3
RC band	0.1	0	0.1	0	0

Fig. 13. Variation in the fundamental frequency after each loading signal

4.1.3. Qualitative analysis of crack

Fig. 14 shows the final state of the three house models after 386 GUA loading. The same house was tested with five different loading signals; therefore, the ultimate damage is the cumulative impact of all the loading applied. However, the three house models were tested using the same standard protocol, so the damage state can be compared to understand the structural behavior and vulnerability to the seismic loading. Several cracks were developed, leading to almost a collapse state for the out-of-plane wall (Fig. 14 (a)). This damage state corresponds to the 'poorly built structure' behavior for seismic intensity VIII on the Modified Mercalli scale (Kramer, 1996). For the house with a timber band, the concentration of cracks was mainly between the band level, except for the thin vertical crack running along the corner of the wall on the right side of the in-plane wall (Fig. 14 (b)). The house model with the RC band had damage localized between the band (Fig. 14 (c)). Both the house models with timber and RC band were standing firmly, which is crucial for preserving human life during earthquakes.

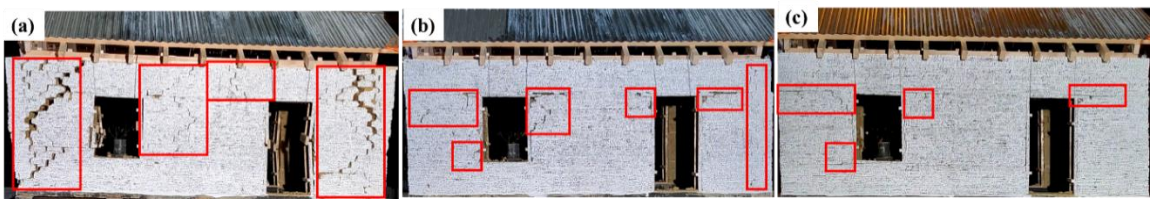

Fig. 14. Location indicating crack concentration after 386%GUA loading in the house without a band (a), with timber band (b), and with RC band (c)

The damage to the in-plane wall near the door opening is compared for all three house models after the final 386GUA signal loading (Fig. 15). Cracks were observed propagating through the interface between the mortar joint and the extruded earth block unit. The house without a band had several wide cracks, leading to the collapse of the out-of-plane wall. In contrast, both houses with bands showed sliding at the interface of the bands, as indicated by arrows in Fig. 15 (at lintel level in the house with a timber band and at the lintel and sill level in the house with an RC band). The cracks are isolated in two sections in the house with the RC band; the area is indicated within a rectangle. The house with the timber band house had a crack running along the corner joint,

which could be due to the ladder-like design of the timber seismic band or the small size of the band. Further testing at the scale of a wall may be necessary to determine the root cause. Despite this, the out-of-plane wall remained intact in the house with a timber seismic band.
In the case of a house with a seismic band, the crack size was within the repairable range. This shows that the seismic band helps to maintain the structural integrity even after multiple loading signals. The crack size of 0.5 mm to 5 mm can be repaired using grouting, and for wider cracks of 5 to 25 mm, wire mesh fixing or stitching methods are recommended by the NRA repair and retrofitting manual (NRA, 2017).

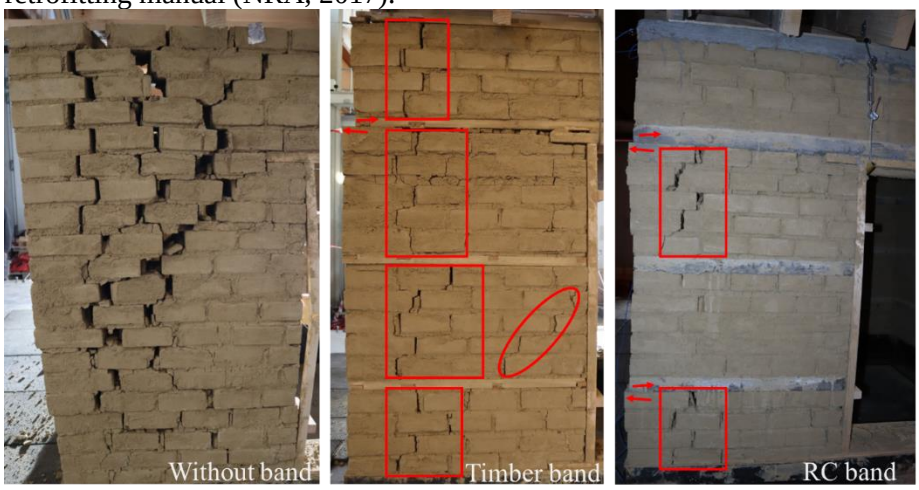

Fig. 15. Failure pattern comparison after 386GUA loading in the in-plane wall portion (next to the door opening)

4.2. In-plane wall

4.2.1. Equivalent Viscous Damping Ratio

EVDR is calculated by taking an average of results from all four accelerometers $BA_{1\text{-}4}$ as shown in Fig. 6.The half-Power (bandwidth) method is used to determine the EVDR using the frequency response curve (F. Vieux-Champagne et al., 2017). This method is one of the most convenient approaches, where the damping ratio is determined using the frequencies at response amplitude corresponding to the level $1/\sqrt{2}$ times its peak value (Clough & Penzien, 2003). Fig. 16 compares the EVDR variation after each loading signal for the three house models. The error bars indicated on the curve is the value of standard deviation. The EVDR values tend to decrease initially and then gradually increase with the damage. The low EVDR value for the house without a band at 273 GUA is due to a big difference in measurement from each corner of the building. The curves for the house with timber and RC band are comparable because of the sliding mechanism at the lintel band level in both cases. The house with timber band has a higher EVDR value, about 65% higher than the house with the RC band.

4.2.2. Acceleration amplification factor

The amplification factor is given by the ratio of peak acceleration recorded at the top of the wall to that applied on the shake table. The peak acceleration recorded by four accelerometers placed on the wall top (Fig. 6 (a)) is used to calculate the amplification factor. The positioning of the accelerometers was at the corner of the structures; thus, the measured values correspond to that for the in-plane wall.
Fig. 17 represents the variation of amplification factor during each loading signal for the three house models. The average amplification value is calculated by taking the peak acceleration measured by each accelerometer and dividing it by the peak acceleration applied to the shake

table. The error bars in the graph indicate the standard deviation value, which can increase due to structural damage causing a difference in displacement rate. For both timber and RC band house models, the amplification follows the declining trend, which is due to easily sliding of the top part of the structure after the interface at the lintel band is damaged. The amplification increases with the increasing loading signal for the house without a band and then decreases after the 240 GUA signal. The standard deviation (SD) for the house without a band is high because of extensive damage to the structure after each loading signal. The SD is lower for house with timber band and quite low for that with RC band, indicating an enhanced paraseismic behavior. Therefore, the seismic band helps to reduce overall amplification at the top of the structure by allowing each section to slide as an individual block.

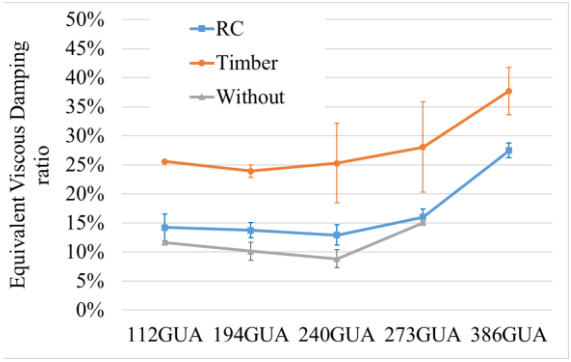

Fig. 16. EVDR variation after each loading cycle

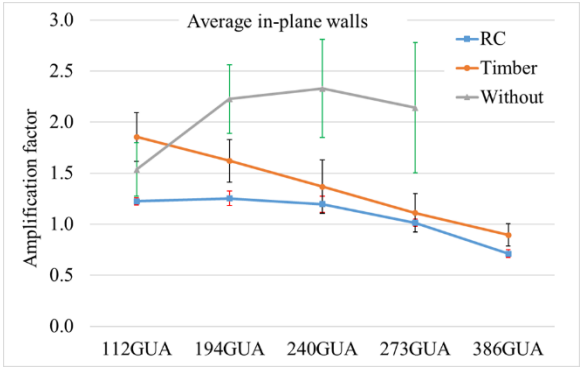

Fig. 17. Average in-plane walls acceleration amplification at various loading

4.2.3. Hysteresis behavior and energy dissipation

The main source of energy loss is due to sliding at the interface. The expected location of maximum sliding is at the band interface with adjacent layers. The overall relative displacement of structure as 112% Guadeloupe signal (see Fig. 24b) was not significant enough to compare the response of three house models at each band level. Therefore, to compare the response of three house models, the hysteresis behavior and energy dissipation calculation are made for the three house models at 194% Guadeloupe signal, as it provides a representative behavior of the structure where the effect of earlier loading cycle was minimal. A region on the right side of the in-plane wall is selected to determine the energy dissipation, as shown in Fig. 18. Bands 1-4 are marked at different levels of band, which will be referred to in the calculation and analysis. The displacement and acceleration markers indicate the locations where results from the DIC were extracted.

The following steps were used to obtain the hysteresis curve and calculate the energy dissipation at each band level.

Step 1: Displacement and acceleration values were extracted from the DIC at specific locations indicated in Fig. 18.

Step 2: Average values for displacement and acceleration calculated at each level

Step 3: Calculation of force and lateral drift

Force_interband = interband_section mass × interband section average acceleration

Lateral_drift = difference between the average top and bottom displacement for each interband section

Step 4: Obtaining the hysteresis curve by plotting the lateral drift and force for each interband section. The sample hysteresis curve is shown in Fig. 19 (left), which is difficult to understand.

Step 5: To obtain the energy dissipation, the force-displacement data were discretized at 1 second time interval and the area under the curve and the cumulative displacement were calculated. The sample plot for cumulative energy vs. cumulative displacement is given in Fig. 19 (right).

Cumulative displacement = sum of absolute displacement from force-displacement data

Cumulative energy = sum of area made by force-displacement curve

Fig. 18. Region selected for energy dissipation with a location represented for displacement and acceleration points

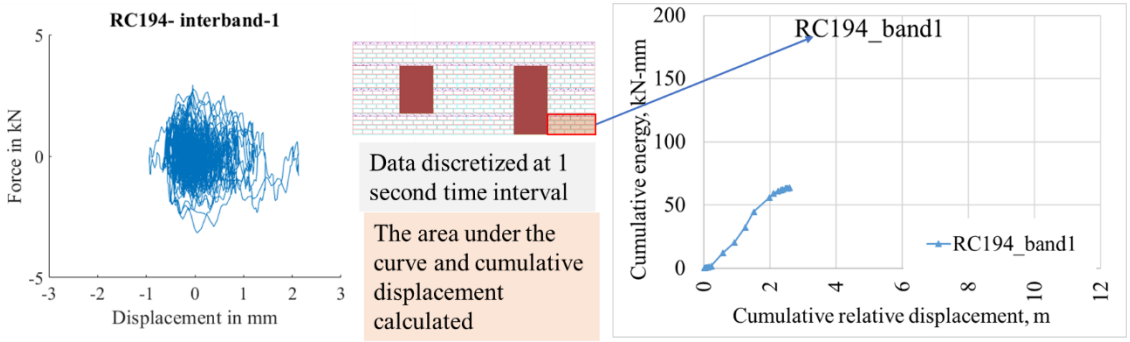

Fig. 19 General steps for obtaining cumulative energy curve

The same approach was applied to all three building models at each band level to obtain the cumulative energy and displacement curve for each inter-band level. Fig. 20 (a) shows the cumulative energy dissipated for the house without a band. For comparison purposes, the band number indicated in the legend corresponds to the same level as the band in the other two houses, even though the house is without a band. The cumulative energy dissipation is highest for the band 3 level, which remained constant from the cumulative displacement of 4 m to 10 m (see Fig. 20 (a)).

Fig. 20 (b) shows the comparison of cumulative energy dissipated at the various inter-band level for the house with a timber band. The energy dissipation for interband-1 and -2 is high with small cumulative displacement. For the interband-3, the energy dissipation increases until 8 m cumulative displacement, then remains constant. The least amount of energy is dissipated by the interband-4. A similar observation is obtained for the house with the RC band (Fig. 20 (c)) with maximum cumulative energy for interband-3 being 180 kN-mm. Also, the energy dissipated by the interband-4 is least in this case. With the damage, the structural capacity decreases, but the structure continues to dissipate energy (damping) with the opening and closing phenomena of the crack (Kayirga & Altun, 2021) and with frictional energy loss due to the sliding mechanism at the interface.

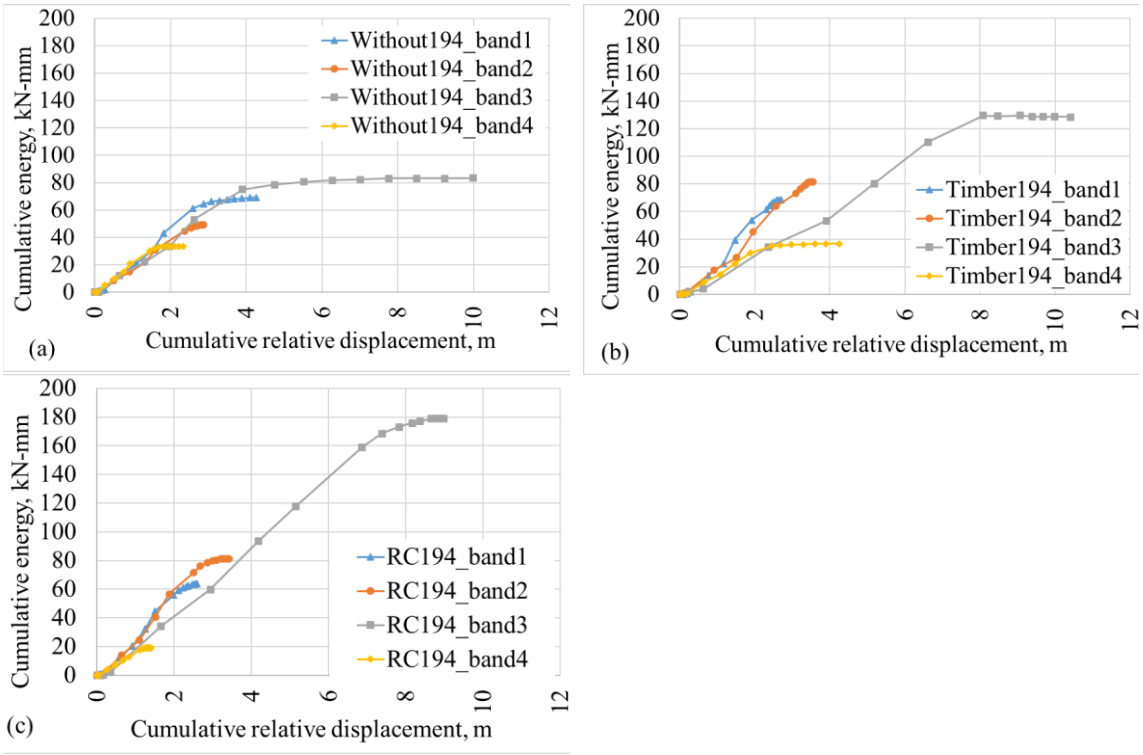

Fig. 20. Cumulative energy dissipation at various inter-band levels for the house (a) without a band, (b) with a timber band, and (c) with an RC band

4.2.4. Principal strain field

The principal strain field is used to visualize the crack formation and its propagation pattern (Salmanpour & Mojsilović, 2013) on the in-plane wall. The major principal strain fields are compared by taking the instant when the maximum strain has occurred during a particular loading signal. The comparison for the 112GUA signal is not covered because of its low impact on the structure.

In Fig. 21, the major principal strain field at 194% Guadeloupe signal at the instant close to 9 s during the loading cycles are compared when the strain concentration on the global surface was maximum. The surface cracks were not visible with naked eyes but thanks to DIC analysis with images from the high-speed camera, the mechanical behaviors of the structures are compared. The strain was seen to be concentrated at the band level for houses with RC and timber bands. Some cracks are initiated in the house with timber band on the section above the lintel band level. The crack is formed diagonally along the corner of the window opening for the house without a band. The initiation of the cracks from three regions on the top section is seen in the house without a band at 194GUA.

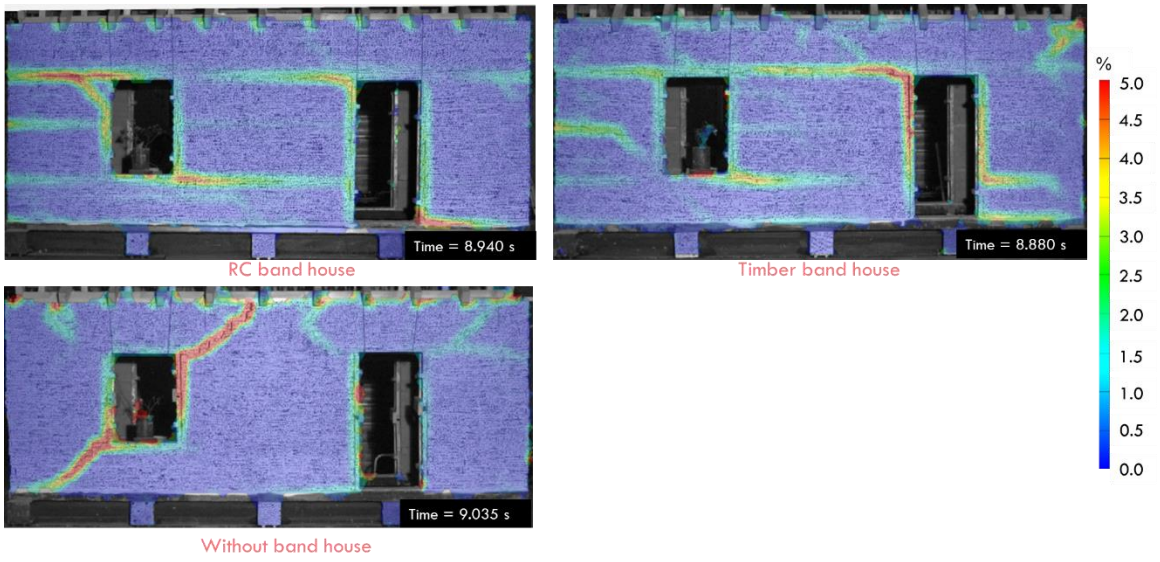

Fig. 21. Major Principal Strain field comparison at 194GUA loading

During Guadeloupe 240% signal (see Fig. 22), the strain increases at the lintel band level for both houses with RC and timber band. At this stage, a new crack was observed to initiate at the bottom section below sill level. The crack that started during 194GUA continues to propagate below the lintel level for the house without the band, and a new crack appears at the sill level next to the door opening (see Fig. 22 in the house without a band).

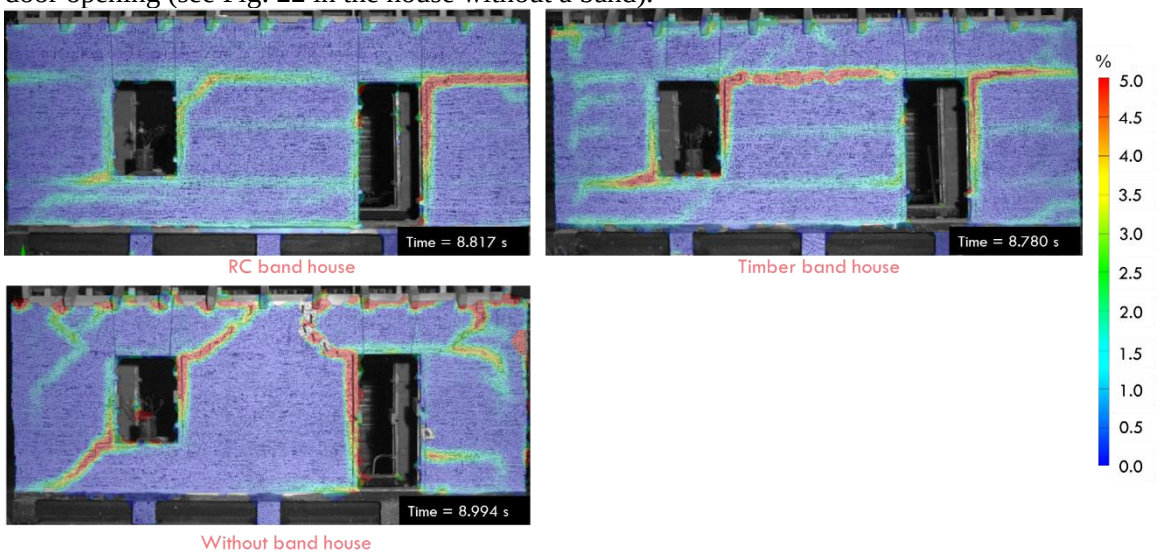

Fig. 22. Major Principal Strain field comparison at 240GUA loading

During 273GUA loading, for the house with RC band, the strain concentration in the section below the sill level is increased, and there is also the initiation of crack on the right bottom part (see Fig. 23 RC band house). For the house with a timber band, cracks in the section above the lintel level are increased along with concentration at the sill level next to the door frame (see Fig. 23 Timber band house). In the house without a band, the crack propagation reached the sill level, and a new diagonal crack formed from the bottom right corner of the window opening (see Fig. 23 without band house). Additionally, the crack size on the right part of the in-plane wall increased for the house without a band.

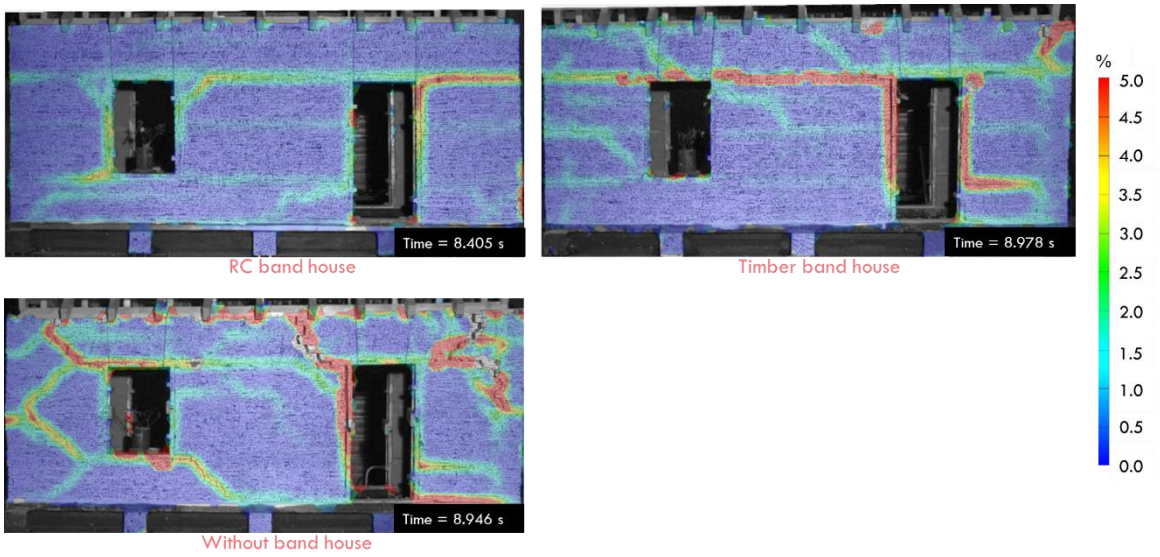

Fig. 23. Major Principal Strain field comparison at 273GUA loading

4.3. Out-of-plane

Out-of-plane (OOP) displacement is obtained from the DWDS placed at the band level on the OOP wall as shown in Fig. 24 (a). DWDS 2, 3, 4, and 5 recorded the absolute displacement of the OOP wall and the relative displacement was calculated by subtracting the table displacement. The maximum relative displacement occurred at DWDS 2, which is located at the free end of the wall. The maximum relative displacement at DWDS 2 was obtained for each house model and the corresponding relative displacement values at DWDS 3, 4, and 5 were extracted to compare the OOP displacement.

Fig. 24 (b-f) consists of a comparison of relative displacement of OOP wall under different loadings. The Y-axis in the graph represents the height from the bottom of the model, and X-axis gives the relative displacement value. A linear plot was used to interpolate the results between consecutive band levels, as DWDS were placed only at four band levels. At the 112GUA signal, all three models behave comparably, but past 194GUA signal, a significant difference in the OOP displacement pattern is noticed. The least maximum OOP displacement occurs in the house with an RC band, followed by the one with a timber band and then without a band house. The displacement at each band level is not following the same line slope as observed in Fig. 24(d-f) for 240GUA, 273GUA, and 386GUA signals, which results from the sliding at the interface between the band and the mortar joints. From these comparisons (Fig. 24), it is evident that the seismic bands help in reducing the maximum displacement of the OOP wall.

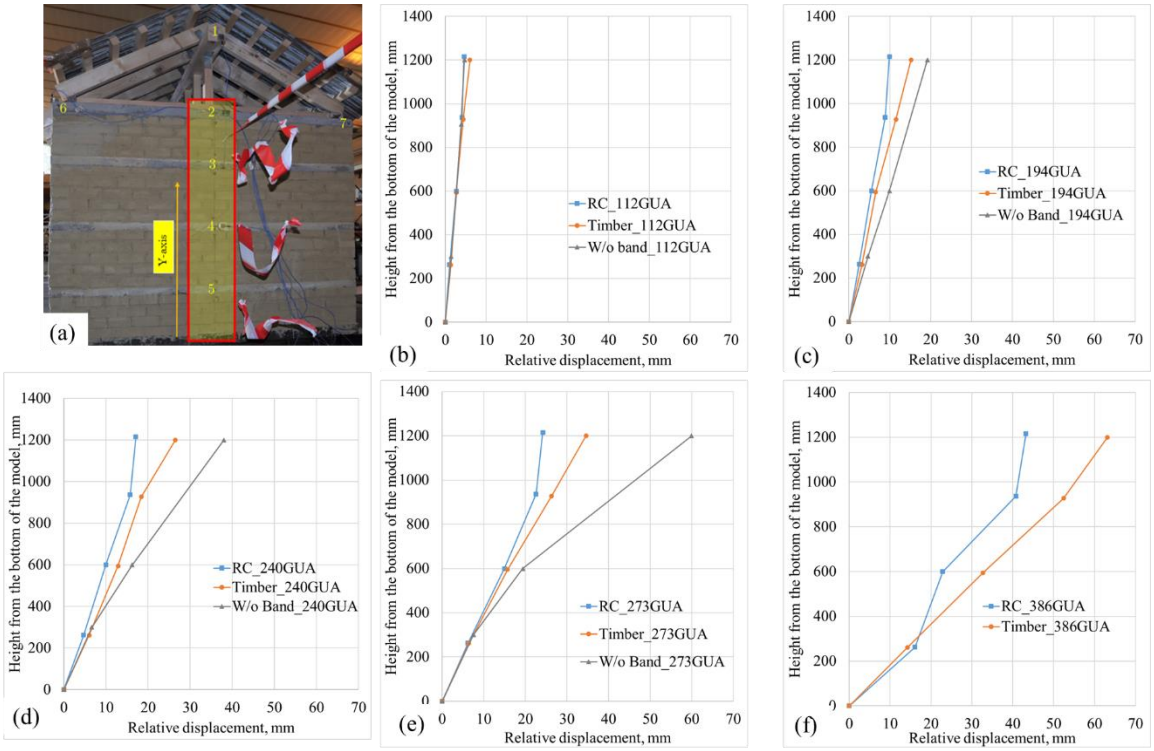

Fig. 24. Out-of-plane displacement along the mid-section of the wall at various loadings

4.4. Sliding at interface

The sliding mechanism at the band interface is the crucial feature of the horizontal seismic band, which helps reduce deflection, increase energy dissipation, and limit crack propagation. The bands were placed at four levels, but their performances varied. To determine the most crucial location of the seismic band with the greatest impact on the structure, the DIC output was used to compare the sliding at the interface. The results from the 194GUA signal were solely used for the house with timber and RC band as it provides comprehensive information about the structure's overall behavior, and there is less influence of earlier damage.
The maximum sliding occurring at the band interface is determined from all data sets, and the corresponding sliding values at other location interfaces are taken at the same instant. The maximum sliding at the band interface was recorded at the time instant corresponding to 9 s on the shake table displacement as indicated in Fig. 1.

Fig. 25 and Fig. 26 show the deformed shape of the house with timber and RC band, respectively. The deformed shape has been scaled up 50 times to have better visualization. The values next to the band indicate the actual displacement due to sliding at the band interface. The text box in 'blue' color represents the sliding at the bottom interface, and the 'brown' color represents that at the top interface.

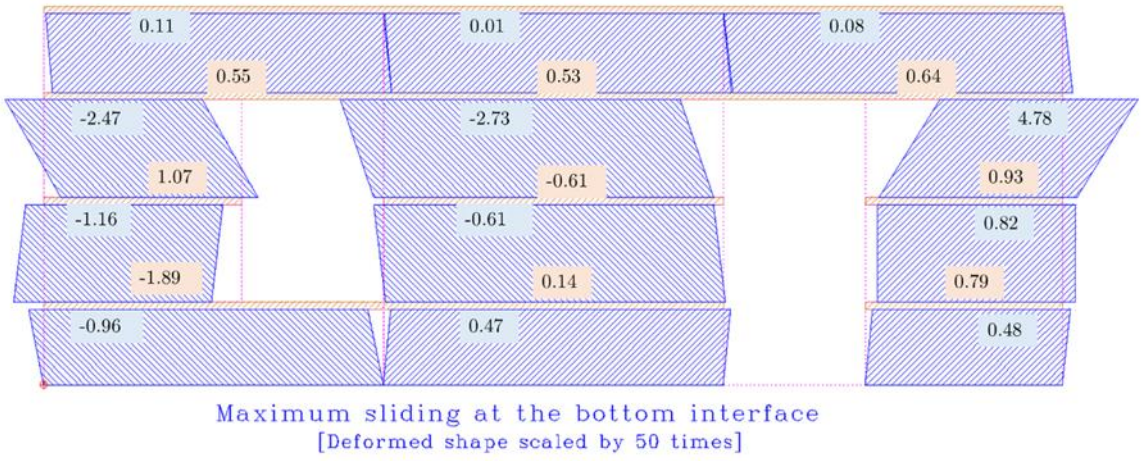

Fig. 25. Deformed shape due to sliding at the band interface in the house with timber band

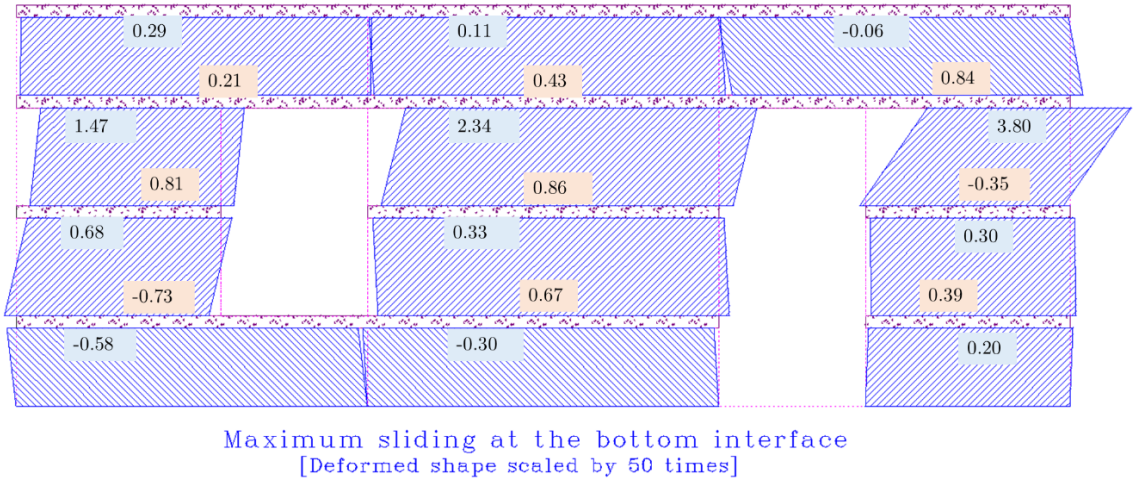

Fig. 26. Deformed shape due to sliding at the band interface in the house with RC band

The maximum sliding occurs at the lintel band level and least at the roof band in both house models. The sliding at sill level interface in the timber band house is also substantial, with a displacement of 1.89 mm at the top interface. These observations are crucial in comprehending the influence of the band at each level. The lintel band is the most critical among the four band levels, as it has a more prominent role in decreasing the structure's overall drift and dissipating energy.

5. Conclusions

The three reduced scale models are tested under dynamic loadings and their performances are compared in this paper. Two types of materials- timber and reinforced concrete are used as a horizontal seismic band, which are commonly used in various parts of the world. Application of the Cauchy law of similitude was applied during specimen preparation and scaling of the applied signal. The speckle patterns created using the array of cotton buds gave contrasting grayscale patterns, which was helpful for DIC analysis. The experimental results are explored using the data captured from accelerometers, DWDS, and DIC. The main conclusions from the dynamic tests on three reduced scale models are as follows:

i. The seismic band application helps reduce the out-of-plane deflection as observed with model house tests, and the acceleration amplification at the top of the structure is lower due to the sliding occurring at the band interface.

ii. The most significant sliding occurs at the lintel band level in both houses with timber and RC band.

iii. The energy dissipation in the structure occurs due to frictional loss, damping, opening, and closing of the cracks. All three house models were prepared from the same material and the only difference with the application of seismic band at four levels.

iv. The DIC strain field results helped understand the path of crack propagation during the dynamic test and highlighted the benefit of seismic bands in limiting the crack propagation and preventing corner separation.

The house model with RC band outperformed as compared to that of the house with timber band, which could be due to the differences in surface area in contact with the wall section and the friction coefficient. The dimension of timber band is not the same as RC band, so there are possibilities of enhancing the performance of timber band but not much for RC (changing shape or preparation process is difficult). Therefore, further investigation is required to better understand the technique to enhance the earthquake-resistant behavior of masonry structures with the application of a horizontal seismic band by optimizing the band size, material, and connection details. Stereo-vision digital image correlation is also important in exploring the complete behavior of out-of-plane wall and the behavior interaction at the corner. Also, the selection of materials for seismic bands depends upon socio-techno-economical aspects, where interdisciplinary stakeholders play an important role. The use of RC seismic band can be convenient in cities where cement is affordable and readily available but not in rural places with less access to roads and goods. Thus, this study highlights the potential for timber seismic band as a cost-effective, life-saving solution for earthquake-resistant masonry structures. The experimental results presented in this study have the potential to raise awareness among various stakeholders worldwide and emphasize the necessity of using seismic bands in masonry structures to ensure safety during earthquakes.

Acknowledgements

This work has been realized in the framework of the LABEX AE&CC and the IDEX CDP Risk @ Université Grenoble Alpes as part of the program "Investissements d'Avenir" overseen by the French National Research Agency (reference: ANR-15-IDEX-02). The authors are grateful for the support from five master's students (UGA-PhITEM), who helped during the construction of the house models. The authors would like to thank and acknowledge the team from FCBA, Bordeaux, for their support during the planning and execution stages of the tests.

References

Adhikari, R. K., Vatteri, A. P., & D'Ayala, D. (2023). Seismic performance assessment of low-rise unreinforced and confined brick masonry school buildings using the applied element method. *Buildings*, *13*, 159. https://doi.org/10.3390/buildings13010159

Aranguren, J., Vieux-champagne, F., Duriez, M., & Aubert, J. (2020). Experimental analysis of timber inclusions effect on paraseismic behavior of earth masonry walls. *Engineering Structures*, *212*(January), 110429. https://doi.org/10.1016/j.engstruct.2020.110429

Arya, A. S., Boen, T., Ishiyama, Y., Martemianov, A. I., Meli, R., Scawthorn, C., … Yaoxian, Y. (2004). Guidelines for Earthquake Resistant Non-Engineered Construction. National Information Centre of Earthquake Engineering.

Banerjee, S., Nayak, S., & Das, S. (2021). Seismic performance enhancement of masonry building models strengthened with the cost-effective materials under bi-directional excitation. *Engineering Structures*, *242*(April), 112516. https://doi.org/10.1016/j.engstruct.2021.112516

Barbacci, N. (2020). Earthen Architecture – Valorisation and Underestimation. *ISPRS - International Archives of the Photogrammetry, Remote Sensing and Spatial Information Sciences*, *XLIV-M-1–2*(September), 1073–1080. https://doi.org/10.5194/isprs-archives-

xliv-m-1-2020-1073-2020
Bhanulatha, G. N. (2018). Experimental Investigation on Utilize Stabilized Adobe Masonry Construction Material. *International Journal for Research in Applied Science and Engineering Technology*, *6*(4), 999–1006. https://doi.org/10.22214/ijraset.2018.4170
Blondet, M., Tarque, N., & Vargas, J. (2018). Using a nylon rope mesh as seismic reinforcement for earthen constructions. In *Kerpic '18 Back to earthen Architecture: Industrialized, Injected, rammed, Stabilized* (pp. 51–58). Turkey: Hasan Kalyoncu University.
Bothara, J., Ahmad, N., Ingham, J., & Dizhur, D. (2019). Experimental Seismic Testing of Semi-Reinforced Stone Masonry Building in Mud Mortar. In *Pacific Conference on Earthquake Engineering*. Auckland, New Zealand.
Bothara, J., & Brzev, S. (2011). *A Tutorial: Improving the Seismic Performance of Stone Masonry Buildings*. Oakland,CA, USA: Earthquake Engineering Research Institute.
Boudaud, C., Baroth, J., & Daudeville, L. (2016). Influence of joist strength variability in timber-frame structures: Propagation of uncertainty through shear wall FE models under seismic loading. *Canadian Journal of Civil Engineering*.
Castellano, A., Fraddosio, A., Oliveira, D. V., Piccioni, M. D., Ricci, E., & Sacco, E. (2023). An effective numerical modelling strategy for FRCM strengthened curved masonry structures. *Engineering Structures*, *274*. https://doi.org/10.1016/j.engstruct.2022.115116
Castillo, E. del R., Allen, T., Henry, R., Griffith, M., & Ingham, J. (2019). Digital image correlation (DIC) for measurement of strains and displacements in coarse, low volume-fraction FRP composites used in civil infrastructure. *Composite Structures*, *212*, 43–57. https://doi.org/10.1016/j.compstruct.2019.01.024
Clough, R. W., & Penzien, J. (2003). *Dynamics of structures*. *Computers and Structures Inc.* Berkeley, California. https://doi.org/10.1139/l90-078
Dalalbashi, A., Ghiassi, B., & Oliveira, D. V. (2021). A multi-level investigation on the mechanical response of TRM-strengthened masonry. *Materials and Structures/Materiaux et Constructions*, *54*(6). https://doi.org/10.1617/s11527-021-01817-4
DUDBC. (2015). *Design Catalogue for Reconstruction of Earthquake Resistant Houses*. (DUDBC, Ed.) (Vol. 1). Kathmandu, Ne: Government of Nepal.
Duriez, M., Vieux-Champagne, F., Trad, R., Maillard, P., & Aubert, J. E. (2020). A methodology for the mix design of earth bedding mortar. *Materials and Structures/Materiaux et Constructions*, *53*(1). https://doi.org/10.1617/s11527-020-1443-9
Eurocode-6. Design of masonry structures- Part-1-1: General rules for reinforced and unreinforced masonry structures, 1 European Committee for Standardization § (2005).
Gaetano, D., Greco, F., Leonetti, L., Lonetti, P., Pascuzzo, A., & Ronchei, C. (2022). An interface-based detailed micro-model for the failure simulation of masonry structures. *Engineering Failure Analysis*, *142*. https://doi.org/10.1016/j.engfailanal.2022.106753
Gautam, D., Rodrigues, H., Bhetwal, K. K., Neupane, P., & Sanada, Y. (2016). Common structural and construction deficiencies of Nepalese buildings. *Innovative Infrastructure Solutions*, *1*(1), 1–18. https://doi.org/10.1007/s41062-016-0001-3
Ghezelbash, A., Beyer, K., Dolatshahi, K. M., & Yekrangnia, M. (2020). Shake table test of a masonry building retrofitted with shotcrete. *Engineering Structures*, *219*(June), 110912. https://doi.org/10.1016/j.engstruct.2020.110912
Gülkan, P., & Langenbach, R. (2004). The Earthquake Resistance of Traditional Timber and Masonry Dwellings in Turkey. *13th World Conference on Earthquake Engineering*, (2297).
Harris, H. G., & Sabnis, G. M. (1999). Structural Modeling and Experimental Techniques. In *CRC Press* (pp. 42–81). CRC Press.
Hofmann, M. (2015). *Le facteur séisme dans l'architecture vernaculaire . Un décryptage entre déterminants culturels , types de structures et ressources cognitives parasismiques*.
IS13828. Improving earthquake resistance of low strength masonry building-Guidelines (1993). India: Bureau of Indian Standard.
Jafari, S., Rots, J. G., & Esposito, R. (2022). A correlation study to support material characterisation of typical Dutch masonry structures. *Journal of Building Engineering*, *45*. https://doi.org/10.1016/j.jobe.2021.103450
Kayirga, O. M., & Altun, F. (2021). Investigation of earthquake behavior of unreinforced masonry

buildings having different opening sizes: Experimental studies and numerical simulation. *Journal of Building Engineering*. https://doi.org/10.1016/j.jobe.2021.102666

Khadka, B., & Shakya, M. (2021). Seismic characteristics of unreinforced mud masonry houses in Nepal: A miserable scenario before and after 2015 Gorkha (Nepal) earthquake. *Engineering Failure Analysis*, *124*. https://doi.org/10.1016/j.engfailanal.2021.105308

Kramer, S. L. (1996). *Geotechnical Earthquake Engineering*. New Jersey: Prentice Hall.

Lan, G., Wang, Y., Xin, L., & Liu, Y. (2020). Shear test method analysis of earth block masonry mortar joints. *Construction and Building Materials*, *264*, 119997. https://doi.org/10.1016/j.conbuildmat.2020.119997

Langenbach, R. (2002). Survivors in the Midst of Devastation: Traditional Timber and Masonry Construction in Seismic Areas. In *Seventh U.S. National Conference on Earthquake Engineering (7NCEE): urban earthquake risk*.

Liang, R., Stanislawski, D., & Hota, G. (2011). Structural Responses of Hakka Rammed Earth Buildings. *International Symposium on Innovation & Sustainability in Civil Engineering*.

Mendes, N., Lourenço, P. B., & Campos-Costa, A. (2013). Shaking table testing of an existing masonry building: assessment and improvement of the seismic performance. *Earthquake Engineering and Structural Dynamics*, *43*, 247–266. https://doi.org/10.1002/eqe.2342

Nadim, F., Moghtaderi-Zadeh, M., Lindholm, C., Andresen, A., Remseth, S., Bolourchi, M. J., … Tvedt, E. (2004). The Bam earthquake of 26 December 2003. *Bulletin of Earthquake Engineering*, *2*(2), 119–153. https://doi.org/10.1007/s10518-004-2286-4

NBC203. Guidelines for earthquake resistant building construction: Low strength masonry (2015). Nepal: Department of Urban Development and Building Construction.

NRA. (2017). *Repair and Retrofitting Manual for Masonry Structure*. Kathmandu, Nepal.

Ortega, J., Vasconcelos, G., & Correia, M. R. (2015). Seismic-resistant building practices resulting from Local Seismic Culture. *Seismic Retrofitting: Learning from Vernacular Architecture*, (August 2016), 17–22. https://doi.org/10.1201/b18856-5

Papagiannopoulos, G. A., & Hatzigeorgiou, G. D. (2011). On the use of the half-power bandwidth method to estimate damping in building structures. *Soil Dynamics and Earthquake Engineering*, *31*(7), 1075–1079. https://doi.org/10.1016/j.soildyn.2011.02.007

Papanicolaou, C. G., Triantafillou, T. C., Karlos, K., & Papathanasiou, M. (2007). Textile-reinforced mortar (TRM) versus FRP as strengthening material of URM walls: in-plane cyclic loading. *Materials and Structures*, *40*(10), 1081–1097. https://doi.org/10.1617/s11527-006-9207-8

Petry, S., & Beyer, K. (2014). Scaling Unreinforced Masonry for Reduced-scale Seismic Testing. *Bulletin of Earthquake Engineering*, *12*(6), 2557–2581. https://doi.org/10.1007/s10518-014-9605-1

Rafi, M. M., Lodi, S. H., Qazi, S. A., Kumar, A., & Verjee, F. (2018). Seismic response of reduced scale stone masonry building. In *Proceedings of the Institution of Civil Engineers - Structures and Buildings* (Vol. 171, pp. 528–541). https://doi.org/10.1680/jstbu.16.00031

Reyes, J. C., Smith-Pardo, J. P., Yamin, L. E., Galvis, F. A., Sandoval, J. D., Gonzalez, C. D., & Correal, J. F. (2019). In-plane seismic behavior of full-scale earthen walls with openings retrofitted with timber elements and vertical tensors. *Bulletin of Earthquake Engineering*, *17*, 4193–4215. https://doi.org/10.1007/s10518-019-00601-8

Salmanpour, A. H., & Mojsilović, N. (2013). Application of Digital Image Correlation for strain measurements of large masonry walls. In *Proceedings of the 5th Asia Pacific Congress on Computational Mechanics*. Singapore.

Sathiparan, N., Mayorca, P., & Meguro, K. (2012). Shake table tests on one-quarter scale models of masonry houses retrofitted with PP-band mesh. *Earthquake Spectra*, *28*(1), 277–299. https://doi.org/10.1193/1.3675357

Shrestha, H., Pradhan, S., & Guragain, R. (2012). Experiences on Retrofitting of Low Strength Masonry Buildings by Different Retrofitting Techniques in Nepal. *15th World Conference on Earthquake Engineering, Lisbon Portugal*.

Sieffert, Y., Vieux-Champagne, F., Grange, S., Garnier, P., Duccini, J. C., & Daudeville, L. (2016). Full-field measurement with a digital image correlation analysis of a shake table test on a timber-framed structure filled with stones and earth. *Engineering Structures*, *123*, 451–

472. https://doi.org/10.1016/j.engstruct.2016.06.009
Stazi, F., Serpilli, M., Chiappini, G., Pergolini, M., Fratalocchi, E., & Lenci, S. (2020). Experimental study of the mechanical behaviour of a new extruded earth block masonry. *Construction and Building Materials*, *244*. https://doi.org/10.1016/j.conbuildmat.2020.118368
Tomaževič, M. (2009). Shear resistance of masonry walls and Eurocode 6: shear versus tensile strength of masonry. *Materials and Structures*, *42*(7), 889–907. https://doi.org/10.1617/s11527-008-9430-6
UN-Habitat, L'urgence, A. de, & NSET-Nepal. (2006). *Guidelines for Earthquake-Resistant Construction of Non-Engineered Rural and Sub Urban Houses in Pakistan*. Pakistan.
Vieux-Champagne, F., Sieffert, Y., Grange, S., Belinga Nko'ol, C., Bertrand, E., Duccini, J. C., … Daudeville, L. (2017). Experimental analysis of a shake table test of timber-Framed structures with stone and earth infill. *Earthquake Spectra*, *33*(3), 1075–1100. https://doi.org/10.1193/010516EQS002M
Vieux-Champagne, Florent. (2013). *Analyse de la vulnérabilité sismique des structures à ossature en bois avec remplissage*. Universite Grenoble Alpes.
Vlachakis, G., & Kleanthi, M. (2020). Learning from failure: Damage and Failures of Masonry Structures, after the 2017 Lesvos earthquake (Greece). *Engineering Failure Analysis*. https://doi.org/10.1016/j.engfailanal.2020.104803
Wang, M., Liu, K., Guragain, R., Shrestha, H., & Ma, X. (2018). Shake table tests on the two - storey dry - joint stone masonry structures reinforced with timber laces and steel wires. *Bulletin of Earthquake Engineering*, *17*, 2199–2218. https://doi.org/10.1007/s10518-018-00528-6
Wang, M., Liu, K., Lu, H., Shrestha, H., Guragain, R., Pan, W., & Yang, X. (2017). In-plane cyclic tests of seismic retrofits of rubble-stone masonry walls. *Bulletin of Earthquake Engineering*, *16*(5), 1941–1959. https://doi.org/10.1007/s10518-017-0262-z
Yadav, S., Damerji, H., Keco, R., Sieffert, Y., Crété, E., Vieux-Champagne, F., … Malecot, Y. (2021). Effects of horizontal seismic band on seismic response in masonry structure: Application of DIC technique. *Progress in Disaster Science*, *10*, 100149. https://doi.org/10.1016/j.pdisas.2021.100149
Yadav, S., Sieffert, Y., Crété, E., Vieux-Champagne, F., & Garnier, P. (2018). Mechanical behaviour of different type of shear band connections being used in reconstruction housing in Nepal. *Construction and Building Materials*, *174*, 701–712. https://doi.org/10.1016/j.conbuildmat.2018.04.121
Yadav, S., Sieffert, Y., Vieux-champagne, F., Debove, L., Decret, D., Malecot, Y., & Garnier, P. (2022). Optimization of the Use Time of a Shake Table with Specimen Preparation outside the Table Surface. *Buildings*, *12*(3), 319. https://doi.org/10.3390/buildings12030319